# Curvature Dynamics of a Coastal Barotropic Outflow Jet on a Slope

WALTER I. TORRES[a] AND JAMES L. HENCH[b]

[a] *Applied Physics Laboratory, University of Washington, Seattle, Washington*
[b] *Marine Laboratory, Nicholas School of the Environment, Duke University, Beaufort, North Carolina*

ABSTRACT: This study adopts a curvature dynamics approach to understand and predict the trajectory of an idealized depth-averaged barotropic outflow onto a slope in shallow water. A novel equation for streamwise curvature dynamics was derived from the barotropic vorticity equation and applied to a momentum jet subject to bottom friction, topographic slope, and planetary rotation. The terms in the curvature dynamics equation have a natural geometric interpretation whereby each physical process can influence the flow direction. It is shown that a weakly spreading jet onto a steep slope admits the formulation of a 1D ordinary differential equation system in a streamline coordinate system, yielding an integrable ordinary differential equation system that predicts the kinematical behavior of the jet. The 1D model was compared with a set of high-resolution idealized depth-averaged circulation model simulations where bottom friction, planetary rotation, and bottom slope were varied. Favorable performance of the 1D reduced physics model was found, especially in the near field of the outflow. The effect of nonlinear processes such as topographic stretching and bottom torque on the fate of the jet outflow is explained using curvature dynamics. Even in the tropics, planetary rotation can have a surprisingly strong influence on the near-field deflection of an intermediate-scale jet, provided that it flows across steep topography.

KEYWORDS: Jets; Vorticity; Coastal flows; Barotropic flows; Idealized models; Ocean models

## 1. Introduction

Well-mixed (or nearly barotropic) outflows onto sloped bathymetry are common geophysical phenomena including rip currents, tidal inlet jets, flows through straits, and wave-driven jets through channels on coral reefs (Talbot and Bate 1987; Wolanski 1988; Symonds et al. 1995; Brun et al. 2020). These circulation features are characterized by steep gradients in water properties such as momentum and density relative to the ambient fluid and can play a key role in transporting scalars in the coastal ocean (Suanda and Feddersen 2015; Moulton et al. 2023). The physical scales of environmental jets determine which forces (inertia, bottom drag, rotation, etc.) affect their behavior. Small-scale outflows have been well studied in engineering literature (Jones et al. 2007), while large-scale jets have been examined in geophysical fluid dynamics studies (Flexas et al. 2005). Well-mixed environmental outflows like reef pass jets and rip currents, however, can occur at intermediate transport and horizontal scales of $\mathcal{O}(1-1000)\,\mathrm{m^3\,s^{-1}}$ and $\mathcal{O}(0.1-10)\,\mathrm{km}$, respectively (Talbot and Bate 1987; Hench et al. 2008). Recent work has highlighted the importance of analogous small-to-intermediate-scale buoyant environmental outflows (Hetland and MacDonald 2008; Rodriguez et al. 2018; Basdurak et al. 2020), but intermediate-scale barotropic outflows are still not well understood despite the ramifications for ecosystem function and human safety (Lowe and Falter 2015; Castelle et al. 2016). The trajectory of these outflows in part determines exchange between the near shore and coastal ocean, so understanding the processes behind alongshore deflection and cross-shore penetration of jets is worthwhile.

A key feature of barotropic and stratified outflows alike is that the governing dynamics tend to change along their course, typically understood as a transition from near-field to far-field dynamics as the length and time scales develop (Horner-Devine et al. 2015). In large-scale jets/plumes, the near field can be inertia dominated (Ro > 1), while the far field tends to be rotationally dominated (Ro < 1). Planetary rotation can turn mid- to low- Ro outflows in the near field to eventually orient downcoast as a coastal current. It is not clear a priori how the Coriolis acceleration will affect the solution of intermediate-scale outflows, but it is expected to depend on the relative impact of other coastal ocean dynamical processes such as inertia, topographic gradients, and bottom drag. Small-scale flows are typically inertia–pressure gradient dominated and are negligibly affected by rotation. Bottom friction can influence outflows at a range of scales depending on the jet/plume aspect ratio and bottom drag coefficient (Atkinson 1993; McCabe et al. 2009; Horner-Devine et al. 2015).

Potential vorticity conservation has often been used to study and predict the behavior of outflows, especially in the far field (Whitehead 1985; An and McDonald 2004). The application of potential vorticity conservation can be used to obtain properties such as the width, depth, and transport of the far-field coastal current (Thomas and Linden 2007). Prior analytical solutions for the trajectory and transport of barotropic outflows based on vorticity conservation, however, are not well-behaved on steep slopes, especially in the near-field jet region (Beardsley and Hart 1978). In the near field, deflection and spreading co-occur, and examining individual vorticity components may clarify the kinematics of outflow jets there. Relative vorticity is comprised of shear and curvature

---

*Corresponding author*: Walter I. Torres, wtorres@uw.edu

constituents that arise in a natural coordinate system (Chew 1974). As an outflow jet deflects and spreads over the shelf slope, the curvature and shear vorticity, respectively, undergo transformation and potentially interchange (Chew 1975). Examining the dynamics of the individual shear and curvature relative vorticity constituents, therefore, can identify the physical processes governing the kinematics of a jet. This approach differs from using potential vorticity alone, where the shear and curvature vorticity constituents are combined.

Path equations for comparable geophysical flow features have been derived by considering the curvature vorticity constituent. Curvature vorticity has been used to derive path equations for the meandering of the Gulf Stream, approximated as a free jet over linear topography (Warren 1963). This theoretical model was later extended to describe the trajectory of the weakly nonlinear flow over arbitrary topography, capturing behaviors such as jet trapping, retroflection, and deflection (Cushman-Roisin et al. 1997). Contour dynamics has also been used to predict the trajectory of outflows (Kubokawa 1991; Flierl 1999; Southwick et al. 2017). All of these models, however, assume potential vorticity conservation and do not account for bottom drag. For outflows onto a slope, significant vorticity can be generated and dissipated via bottom friction and topographic interaction, which should be accounted for.

Here, we derive a fully nonlinear dissipative streamwise curvature dynamics equation and analyze the kinematics (i.e., deflection and spreading) of a barotropic jet outflow onto a linear slope in shallow water. From the curvature dynamics equation and continuity equations, we then derive a simplified 1D streamwise system of ordinary differential equations (ODEs) valid for the domain interest—an idealized circular island domain with a linear slope. Then, we evaluate the validity of the 1D analytical model against idealized horizontally two-dimensional depth-integrated (2DH) ocean circulation simulations across a range of bottom slopes, bottom friction, and Coriolis parameter values. In doing so, we are able to identify the influence of key physics on the fate of an outflow jet from the perspective of curvature dynamics, taking a particular interest in the poorly understood nonlinear near-field region.

## 2. Theory

We formulate the dynamics by starting with the depth-averaged 2D shallow water equations for conservation of mass and momentum

$$\frac{\partial \eta}{\partial t} + \nabla \cdot (H\mathbf{u}) = 0, \qquad (1)$$

$$\frac{\partial \mathbf{u}}{\partial t} + \frac{1}{2}\nabla(\mathbf{u} \cdot \mathbf{u}) - \mathbf{u} \times (\omega + f) + \frac{C_D |\mathbf{u}|\mathbf{u}}{H} + g\nabla\eta = 0, \qquad (2)$$

where $\mathbf{u}$ is the depth-averaged velocity vector, $\omega$ is the vertical relative vorticity, $f$ is the Coriolis parameter, $g$ is the gravitational parameter, $C_D$ is the quadratic bottom friction coefficient, $t$ is time, and $H$ is the water column thickness; the sum of the time-invariant bathymetry $h$ and free surface height $\eta(t)$. Lateral momentum diffusion is ignored. Nonlinear advection
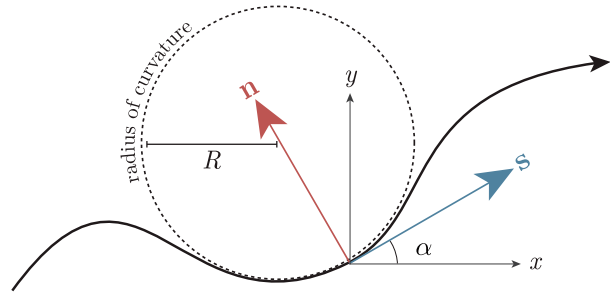


FIG. 1. Schematic of the local streamline coordinate system where the unit vectors $(\hat{\mathbf{s}}, \hat{\mathbf{n}})$ locally define a coordinate system oriented tangent to and perpendicular to the direction of flow $\alpha$, relative to the $x$ direction in Cartesian coordinates. A radius of curvature $R$ is defined as the inverse of flow curvature $(K = 1/R)$. Adapted from Wenegrat and Thomas (2017).

of momentum is formulated as the sum of the Lamb vector and Bernoulli head gradient (Lane et al. 2007) which will later facilitate the derivation of the vorticity equation.

These equations can be recast into a streamwise–streamnormal (or natural) coordinate system, where the unit vectors $(\hat{\mathbf{s}}, \hat{\mathbf{n}})$ are oriented in the direction of and perpendicular to the local flow velocity $\mathbf{u}$, respectively (Hench and Luettich 2003). The flow speed and the Cartesian orientation $(V, \alpha)$ define the velocity vector rather than $(u, v)$ components (Fig. 1):

$$\frac{\partial \eta}{\partial t} + \frac{\partial}{\partial s}(VH) + VH\frac{\partial \alpha}{\partial n} = 0, \qquad (3)$$

$$\frac{\partial V}{\partial t} + V\frac{\partial V}{\partial s} + \frac{C_D V^2}{H} + g\frac{\partial \eta}{\partial s} = 0, \qquad (4)$$

$$V\frac{\partial \alpha}{\partial t} + V^2 K + fV + g\frac{\partial \eta}{\partial n} = 0. \qquad (5)$$

Here, $K$ is the flow curvature which is defined as the along-path change of heading $(\partial\alpha/\partial s = K)$. Taking the curl of (4) and (5) yields the depth-averaged vorticity equation [(6)] where the bottom torque has been expanded into slope torque, speed torque, and dissipation components as in Signell and Geyer (1991):

$$\frac{\partial \omega}{\partial t} + \mathbf{u} \cdot \nabla(\omega + f) + (\omega + f)(\nabla \cdot \mathbf{u}) + \frac{C_D V}{H^2}[\mathbf{u} \times \nabla H] \cdot \hat{\mathbf{k}}$$

$$- \frac{C_D}{H}[\mathbf{u} \times \nabla V] \cdot \hat{\mathbf{k}} + \frac{C_D V \omega}{H} = 0. \qquad (6)$$

We are interested in arranging (6) in terms of the curvature gradient flux $V\partial K/\partial s$ in order to examine the vorticity balance from an intuitive curvature dynamics perspective. To do so, we decompose the vorticity into its shear and curvature constituents [(7)], which arise from the application of the curl operator in the natural coordinate system:

$$\nabla \times \mathbf{u} = \underbrace{-\frac{\partial V}{\partial n}}_{\text{shear}} + \underbrace{VK}_{\text{curvature}}. \qquad (7)$$

Additionally, the horizontal divergence can be decomposed into a speed and diffluence component [(8)] (Bell and Keyser 1993):

$$\nabla \cdot \mathbf{u} = \underbrace{\frac{\partial V}{\partial s}}_{\text{speed}} + \underbrace{V\frac{\partial \alpha}{\partial n}}_{\text{diffluence}}. \tag{8}$$

Using the continuity equation [(3)], the speed divergence can be shown to be equal to the sum of the topographic, diffluence, and unsteady contributions:

$$\frac{\partial V}{\partial s} = -\underbrace{\frac{V}{H}\frac{\partial H}{\partial s}}_{\text{topographic}} - \underbrace{V\frac{\partial \alpha}{\partial n}}_{\text{diffluence}} - \underbrace{\frac{1}{H}\frac{\partial \eta}{\partial t}}_{\text{unsteady}}. \tag{9}$$

After assuming steadiness and substituting (9) into (8), the barotropic vorticity equation [(6)] can be recast as the steady curvature dynamics equation:

$$\underbrace{V\frac{\partial K}{\partial s}}_{\text{curvature gradient flux}} = \underbrace{\frac{\partial}{\partial s}\frac{\partial V}{\partial n}}_{\text{shear divergence}} + \underbrace{VK\frac{\partial \alpha}{\partial n}}_{\text{confluence veering}} - \underbrace{\frac{\partial f}{\partial s}}_{\text{beta effect}}$$

$$+ \frac{1}{H}\frac{\partial H}{\partial s}\left(\underbrace{-\frac{\partial V}{\partial n}}_{\text{shear}} + \underbrace{2VK}_{\text{curvature}} + \underbrace{f}_{\text{Coriolis}}\right)$$
$$\text{stretching}$$

$$- \underbrace{\frac{C_D V}{H^2}\frac{\partial H}{\partial n}}_{\text{slope torque}} + \underbrace{\frac{2C_D}{H}\frac{\partial V}{\partial n}}_{\text{speed torque}} - \underbrace{\frac{C_D VK}{H}}_{\text{dissipation}}, \tag{10}$$

where terms have been named for interpretability. The advantage of (10) is that each term on the right-hand side has a direct effect on the streamwise change in the curvature of a flow streamline, which is physically intuitive (and arguably less opaque than the traditional vorticity equation with respect to flow kinematics). A schematic and description for each of the newly derived terms are provided below (Fig. 2).

*The path equations: A 1D ODE system*

For a coherent momentum jet, the path of its center streamline well approximates the trajectory of the entire feature. With this in mind, we seek to simplify the governing equations in terms of the centerline's path. By considering (10) along the center streamline as defined by the local speed maxima along the jet's trajectory, an inflection point in the velocity profile where $\partial V/\partial n = 0$ (Ochoa and Niiler 2007), one can eliminate terms involving the velocity shear. Additionally considering the problem on an $f$ plane ($\partial f/\partial s = 0$) and assuming that streamlines are parallel close to the centerline ($\partial \alpha/\partial n = 0$) gives

$$\frac{\partial K}{\partial s} = \underbrace{\frac{1}{VH}\frac{\partial H}{\partial s}\left(\underbrace{2VK}_{\text{curvature}} + \underbrace{f}_{\text{Coriolis}}\right)}_{\text{stretching}} - \underbrace{\frac{C_D}{H^2}\frac{\partial H}{\partial n}}_{\text{slope torque}} + \underbrace{\frac{C_D K}{H}}_{\text{dissipation}}. \tag{11}$$

The simplified curvature dynamics reduce to only four terms: curvature stretching, Coriolis stretching, slope torque, and dissipation. Although the assumption of parallel streamlines

precludes jet spreading, usually considered to be a defining feature of momentum jets, we expect the emergent volume balance dynamics to be dominated by the topographic term, where the outflow is fast and the streamwise depth gradient is steep, especially in the near field. One choice for a nondimensional parameter quantifying the primacy of the diffluence and streamwise terms in the continuity equation is $\Upsilon = W\Lambda/(2H_0\alpha_0)$, where $W/2$ is half of the jet width, $\Lambda$ is the slope, $H_0$ is the initial depth, and $\alpha_0$ is the spreading angle. For representative coastal outflows over steep slopes such as coral reef pass jets on some Pacific atolls ($\Lambda > 0.1$, $W/H \approx 10$, $\alpha = \pi/24$), $\Upsilon > 1$, implying the topographic dominance of divergence. For outflows such as rip currents occurring over weak slopes typical of beaches on continental shelves ($\Lambda < 0.01$, $W/H \approx 10$, $\alpha = \pi/24$), $\Upsilon < 1$, implying a diffluential dominance of divergence. Here, we assume $\Upsilon > 1$ and steadiness, which simplifies the continuity equation [(3)] to $\partial V/\partial s = -(V/H)(\partial H/\partial s)$.

We now use the theoretical framework of (11) to study an outflow from an island onto a radially sloping shelf. The island bathymetry is prescribed as

$$h(r) = h_0 + \Lambda(r - R_0), \tag{12}$$

where $\Lambda$ is the bottom slope, $r$ is the radial coordinate relative to the island center ($\theta$ is the azimuthal coordinate), and $R_0$ is the island's radius. After applying polar coordinate transformations (Cushman-Roisin et al. 1997) and assuming $h \gg \eta$, the simplified continuity, curvature, and path equations for the jet on the idealized domain can now be represented by a system of ordinary differential equations:

$$\frac{d\alpha}{ds} = K$$
$$\frac{dr}{ds} = \cos(\alpha - \theta)$$
$$\frac{d\theta}{ds} = \frac{1}{r}\sin(\alpha - \theta)$$
$$\frac{dh}{ds} = \Lambda\frac{dr}{ds}$$
$$\frac{dV}{ds} = -\frac{V}{h}\frac{dh}{ds}$$
$$\frac{dK}{ds} = \frac{1}{h}\frac{dh}{ds}\left(2K + \frac{f}{V}\right) - \frac{C_D}{h^2}\sin(\alpha - \theta) - \frac{C_D K}{h}. \tag{13}$$

Here, $\alpha$ is the flow angle in Cartesian coordinates. Note that these assumptions reduce the dimensionality of the system of equations from 2D to 1D; state variables become a function of along-trajectory distance only. This simplification comes at the cost of neglecting shear vorticity interchange processes and jet deceleration due to spreading. Shear–curvature vorticity interchange, however, requires flow acceleration (Bell and Keyser 1993), and we only consider the steady behavior of a jet here. Next, we evaluate the predictive power of (13) against a high-resolution depth-integrated circulation model with all of the physics represented in (1) and (2). That way, the effect of
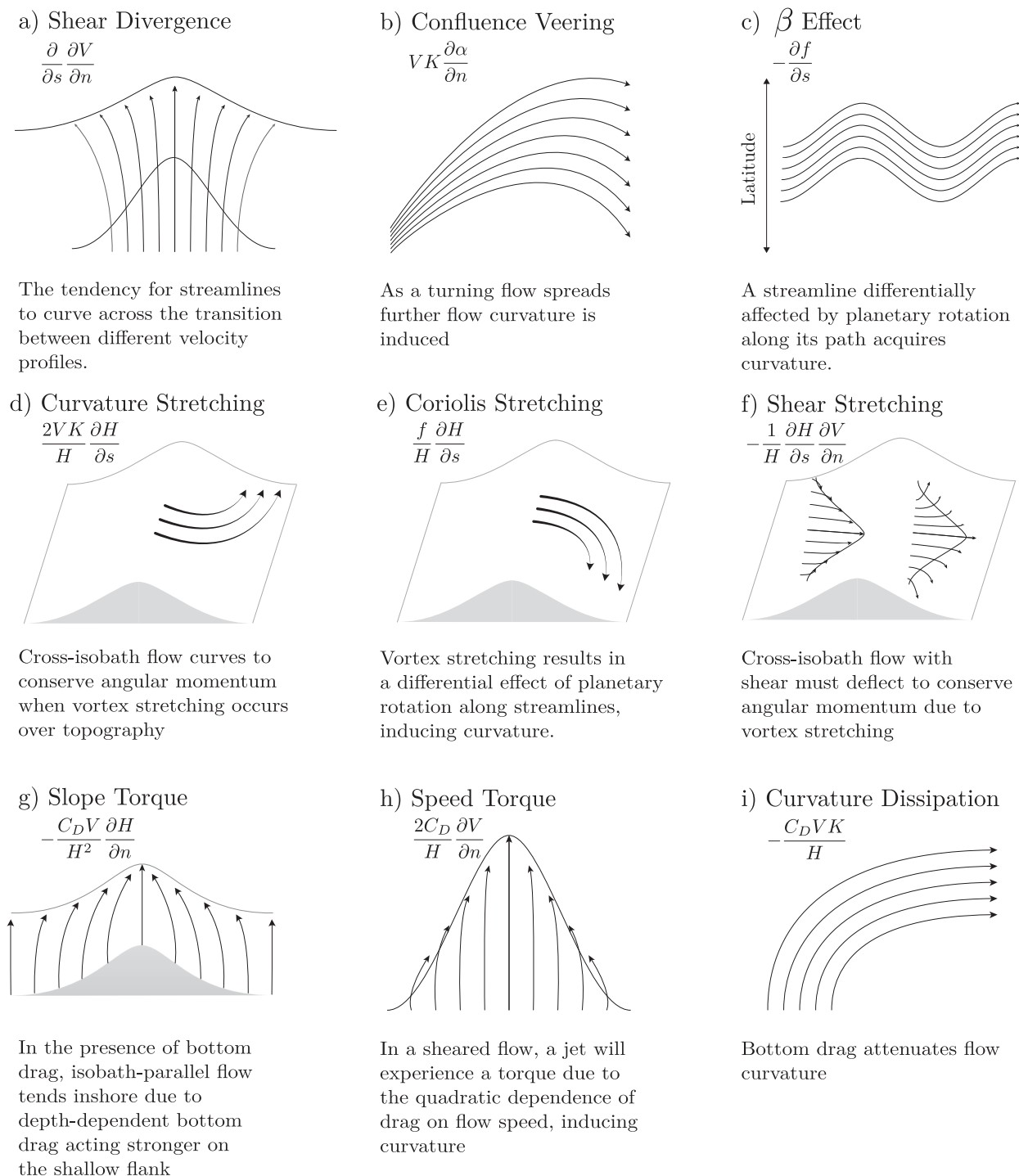
### a) Shear Divergence

$$\frac{\partial}{\partial s}\frac{\partial V}{\partial n}$$

The tendency for streamlines to curve across the transition between different velocity profiles.

### b) Confluence Veering

$$VK\frac{\partial \alpha}{\partial n}$$

As a turning flow spreads further flow curvature is induced

### c) $\beta$ Effect

$$-\frac{\partial f}{\partial s}$$

A streamline differentially affected by planetary rotation along its path acquires curvature.

### d) Curvature Stretching

$$\frac{2VK}{H}\frac{\partial H}{\partial s}$$

Cross-isobath flow curves to conserve angular momentum when vortex stretching occurs over topography

### e) Coriolis Stretching

$$\frac{f}{H}\frac{\partial H}{\partial s}$$

Vortex stretching results in a differential effect of planetary rotation along streamlines, inducing curvature.

### f) Shear Stretching

$$-\frac{1}{H}\frac{\partial H}{\partial s}\frac{\partial V}{\partial n}$$

Cross-isobath flow with shear must deflect to conserve angular momentum due to vortex stretching

### g) Slope Torque

$$-\frac{C_D V}{H^2}\frac{\partial H}{\partial n}$$

In the presence of bottom drag, isobath-parallel flow tends inshore due to depth-dependent bottom drag acting stronger on the shallow flank

### h) Speed Torque

$$\frac{2C_D}{H}\frac{\partial V}{\partial n}$$

In a sheared flow, a jet will experience a torque due to the quadratic dependence of drag on flow speed, inducing curvature

### i) Curvature Dissipation

$$-\frac{C_D VK}{H}$$

Bottom drag attenuates flow curvature

FIG. 2. Schematic diagrams and accompanying interpretations of the curvature dynamics terms in (10).

terms unaccounted for in the reduced physics model (e.g., shear, spreading, unsteadiness, and lateral viscosity) on the curvature gradient flux can be evaluated. Comparable solutions of the ODE system [(13)] were obtained using the Radau IIa implicit Runge–Kutta method implemented in SciPy's solve_ivp function (Virtanen et al. 2020).

## 3. Methods

### a. The idealized domain

For the high-resolution 2D numerical model, the bathymetry was analytically prescribed to be a $\pi/3$ sector of a conical frustum, an island with linearly sloping bathymetry [(12)]. A
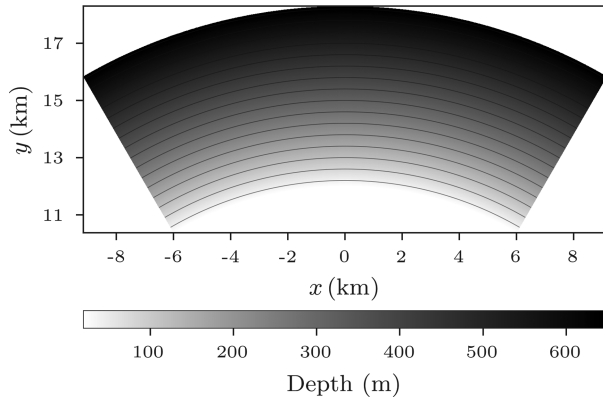
FIG. 3. The bathymetry of the idealized model is a $\pi/3$ sector of a linearly sloping island with the boundary conditions labeled on the edges of the domain. The depth at the inshore boundary is 20 m, and the maximum depth for the steepest slope case ($\Lambda = 0.1$) is 648 m.

polar computational grid was used to discretize the domain geometry (Fig. 3) with $h_0 = 20$ m, $R_0 = 12$ km, and $0.01 \leq \Lambda \leq 0.1$, characteristic of barrier reefs and atolls (Quataert et al. 2015). An inflow boundary condition at the inner radius was specified as a horizontal velocity profile defined by a von Mises distribution function with a negative offset enforcing no net transport across the boundary [(14), (15)]. This emulates how the wave-driven inflow across the reef crest supplies the jet outflow (Herdman et al. 2017) and ensures that the fluid volume of the domain remains constant:

$$Q_r = \int_{-\pi/12}^{\pi/12} u(\theta) d\theta = 0, \tag{14}$$

$$u(r = R_0, \theta) = V_0 a \left[ \frac{e^{\kappa \cos(2\pi\theta/T)}}{2\pi I_0(\kappa)} - b \right]. \tag{15}$$

Here, $V_0$ is the radial velocity, $I_0$ is the zeroth order modified Bessel function, $a$ is a scale parameter, $\kappa$ is a shape parameter controlling the steepness of the profile, $b$ is an offset parameter, $T$ is a periodicity parameter, and $\theta$ is the azimuthal coordinate. The scale, offset, shape, and periodicity parameters ($a = 0.271$, $b = -0.159$, $\kappa = 93.6$, and $T = \pi/6$) were chosen to enforce a net zero mass flux with $\kappa = 93.6$, giving an outflow width of $W = 500$ m.

### b. Numerical model configuration

The depth-integrated equations of motion were solved numerically on this domain with the Regional Ocean Modeling System (ROMS; Shchepetkin and McWilliams 2005) with a uniform density field. A depth-dependent quadratic bottom friction scheme was used corresponding to (4), where $C_D$ is a constant bottom friction coefficient. The harmonic lateral viscosity was set to 0.2 m² s⁻¹, consistent with other coastal oceanographic modeling studies (e.g., Kumar and Feddersen 2017). The simulations were integrated for 10 days with a time step ($\Delta t = 0.25$ s) in order to capture several inertial periods. The Coriolis parameter was set constant throughout the domain

using the *f*-plane approximation. The grid spacing was 15 m in the radial direction and 15–20 m in the azimuthal direction, giving a horizontal computational grid of dimensions ($512 \times 256$). The inflow speed $V_0$ was set to 0.125 m s⁻¹ for all runs, which corresponds to an inflow rate of $Q = 615$ m³ s⁻¹, comparable to large reef pass jets (Herdman et al. 2017) and moderately sized rivers (Cole and Hetland 2016; Lemagie and Lerczak 2020). Radiation boundary conditions for momentum and the free surface were applied at the azimuthal and outer radial boundaries. Model simulations were carried out on the SuperMIC resource through LSU HPC, leveraging the parallelizability of ROMS. Each simulation required about 2500 node-hours, using 160 cores per run. The norm of the domain-integrated kinetic energy was computed to estimate convergence, and all runs were satisfactorily converged ($\delta_{KE}/\|KE\| < 0.01\%$ h⁻¹) after 5 days, after which several inertial periods were captured. As the focus of this paper is on the steady behavior of the flow, model results shown here were time-averaged over the final 3 h of the simulation, similar to the flow time scale given by $\tau = V_0/L_J$, the jet initial velocity divided by the streamwise length scale of interest $L_J \approx 2$ km, over which the jet typically has transitioned from near-field to far-field dynamics.

### c. Numerical experiments

A series of numerical experiments were carried out to explore the dynamics of the coastal outflow using the curvature dynamics equation [(10)]. Of interest are the effects of planetary rotation, shelf topography, and bottom friction. A set of runs was designed to systematically vary the latitude $\phi$, the bottom slope $\Lambda$, and the bottom drag coefficient $C_D$:

$$\phi = [-1.0°, \ -15.0°, \ \mathbf{-30.0°}],$$

$$\Lambda = [0.01, 0.05, \mathbf{0.1}],$$

$$C_D = [0.25, \mathbf{0.125}],$$

where the demonstrative case in bold is examined in detail. Identifying the leading-order dynamical balances of curvature dynamics terms along the center streamline is important for understanding how the jet deflects. For each case, the center streamline of the jet was identified, Eq. (10) was computed, and the ODE system for the jet's path [(13)] was solved.

The ODE system [(13)] was solved using the initial conditions from the circulation model. The initial values $y_0$ were selected to minimize the least squared error between the path of the ODE jet and the path of the jet from the circulation model but only within 10% of $y_0$. SciPy's bounded minimize routine was used (Virtanen et al. 2020). As the ODE system is nonlinear and sensitive to initial conditions, it is possible that there are useful and acceptable solutions in close proximity to nonphysical ones, so providing a narrow range of the initial values is appropriate. For typical parameters, the ODE system is unstable to perturbations about the initial state, as the real parts of the local Lyapunov exponents (the eigenvalues of the linearized Jacobian) are positive. ODE instability combined with the dimensionality of the phase space ($n = 4$) and the presence of nonlinearity suggest that the ODE system
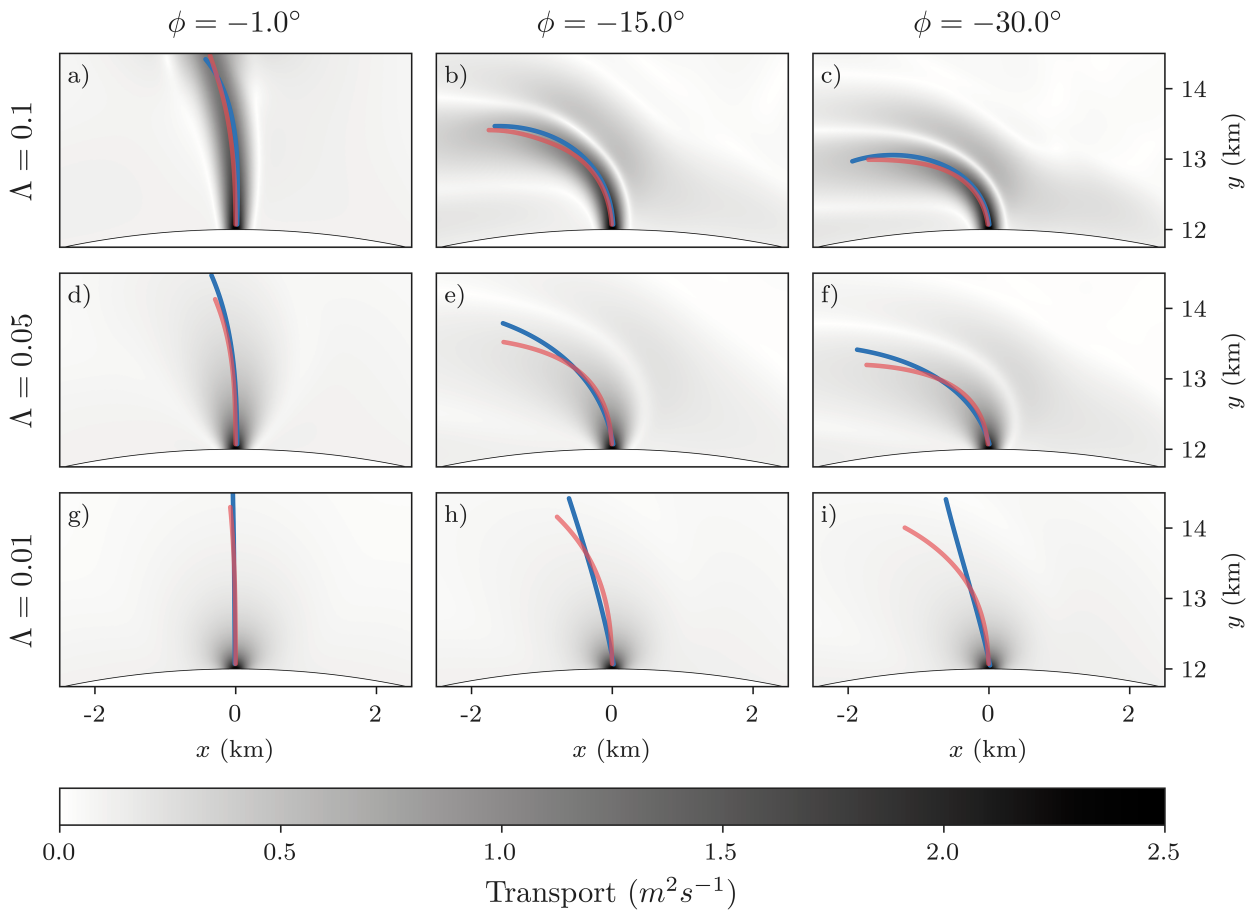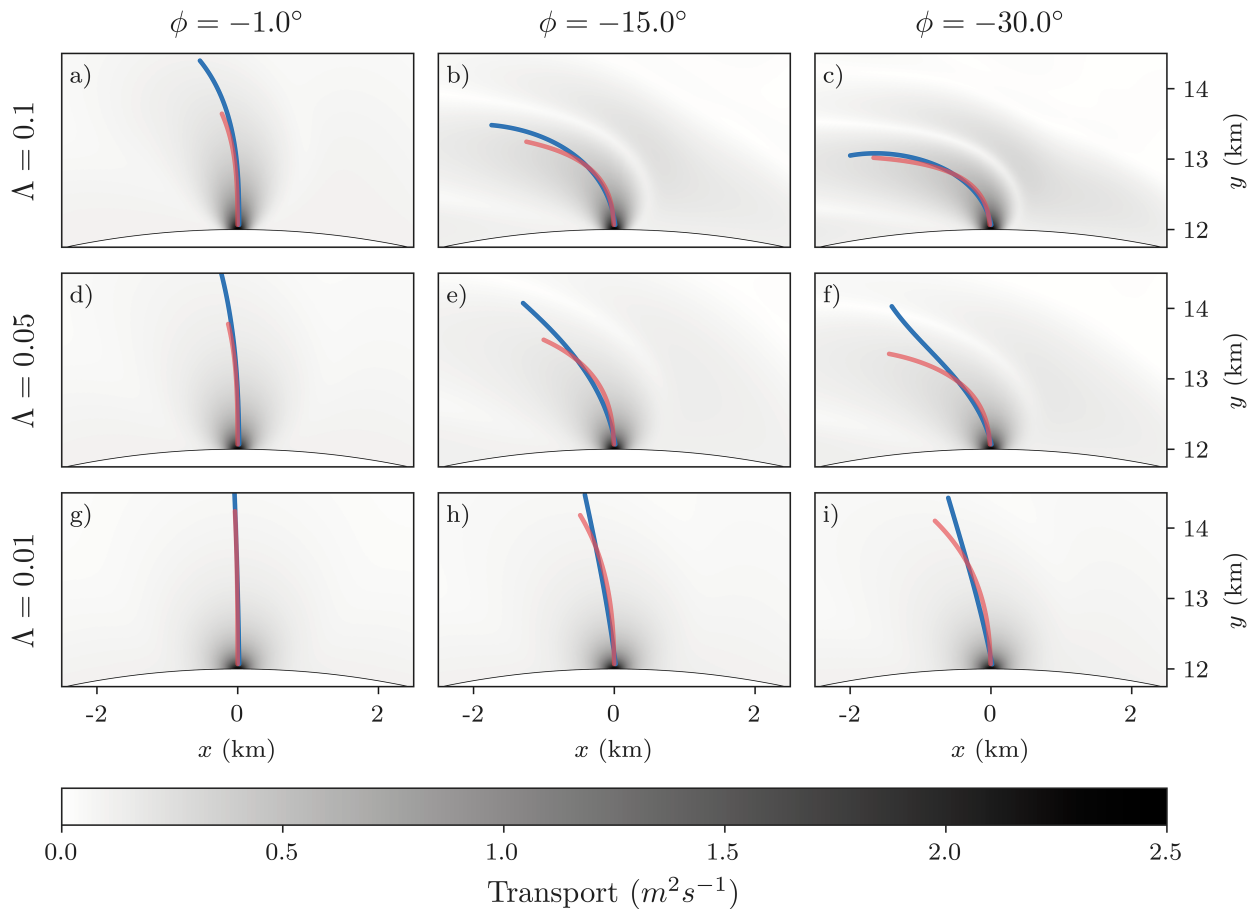
FIG. 4. The depth-integrated transport ($q = VH$), 2DH model-derived center streamline trajectory (red line), and 1D analytical streamline trajectory (blue line) across simulations with $C_D = 0.125$.

is likely to exhibit chaotic properties (Arfken et al. 2013); however, further investigation is beyond the scope of this study.

### d. Center streamline identification

To compare the ODE system with the 2DH numerical model, the center streamline of the simulated jet must be identified. We assume that the center streamline represents the path of the jet. It is also where the 1D ODE system should be most valid. Along this streamline, shear vorticity and diffluence divergence are expected to be at a minimum because this is where an inflection point in the jet velocity profile should occur, and spreading should be relatively stronger on the flanks than the centerline. The jet streamline minimizing the objective function

$$J = \frac{\int_C \left( \left| -\frac{\partial V}{\partial n} \right| + V \left| \frac{\partial \alpha}{\partial n} \right| \right) ds}{\int_C ds} \quad (16)$$

correspondingly minimizes the shear divergence, confluence veering, and speed torque terms in (10), enhancing the viability

of the streamwise ODE system [(11)]. Lagrangian particles were integrated over a static velocity field, i.e., the time average over the final 3 h of simulation defining mean streamlines. The center streamline trajectory was found using the OceanParcels Lagrangian particle tracking package (Delandmeter and van Sebille 2019) in conjunction with Scipy's "minimize_scalar" function (Virtanen et al. 2020) to find the optimal streamline azimuthally along the inner boundary.

## 4. Results

### a. Jet kinematics and trajectories

The set of numerical simulations captured a wide variety of jet behaviors as the model parameters were varied (Figs. 4 and 5). The influence of planetary rotation on the path of the jet was dramatic in simulations with steep bottom slope ($\Lambda = 0.1$). For cases more affected by planetary rotation [$-15°$, $-30°$], typical jet excursions (the cross-shore distance traveled before rectifying to isobaths) were 1–2 km offshore. Despite the relatively high near-field Rossby numbers of the jet (Ro $\approx$ 10), planetary rotation notably deflects the trajectory of the geophysically small jet flowing across a steep

FIG. 5. The depth-integrated transport ($q = VH$), 2DH model-derived center streamline trajectory (red line), and 1D analytical streamline trajectory (blue line) across simulations with $C_D = 0.25$.

slope. The jet stayed coherent and narrow over a larger streamwise distance for low $C_D$ cases, and noticeable spreading does not occur until after the jet is oriented downcoast. For high $C_D$, the jet spreads considerably more in the near field.

The trajectory of the numerically modeled jets compares favorably to predictions of the ODE system [(13)] given similar initial conditions (Fig. 4). It is apparent that the quality of the ODE solutions is best in the near field and departs from the corresponding 2DH solutions with increasing streamwise distance. This is to be expected because key simplifications (i.e., $\Upsilon \gg 1$ and $|VK| \gg |-\partial V/\partial n|$) are inevitably violated when the jet rectifies downcoast along isobaths. The ODE-2DH model agreement was reasonably robust to parameter combinations testing its other core assumptions: parallel streamlines, no velocity shear at the centerline, and steadiness. For larger values of $C_D$, the jet exhibits radially spreading behavior; streamlines diverge from another and the centerline shear vorticity magnitude minimum is not particularly distinct. This implies that the shear vorticity is not weaker than the curvature vorticity, which will be verified later. The ODE system, nonetheless, reasonably recovers the path of the jet in the near field in most cases. 1D ODE solutions on shallow topographic slopes do not perform as well as on steep slopes for most combinations of $C_D$ and $f$, as radial spreading due to friction more readily dominates over topographic divergence in the near field. This allows terms not accounted for in the reduced physics model, such as confluence veering and speed torque, to potentially influence the solution. Thus, the 1D ODE model is most useful under high inertia/low drag conditions.

Having demonstrated the ability of the reduced physics model to predict jet trajectory, we now examine the validity of the assumptions made in its derivation by examining the vorticity, divergence, and curvature budgets of the numerical model output. We select a representative case from the suite of runs to examine in detail, where the influences of the curvature terms in (10) on the jet are clearly illustrated and consistent with the simplifying assumptions: a steep slope, strong planetary rotation, and relatively weak bottom friction [$\phi = -30°$, $\Lambda = 0.1$, $C_D = 0.125$] (Fig. 6). Over a path distance of 2 km, the jet orients as a coastal current downcoast after a ~1-km cross-shelf excursion. A return flow is present on both sides of the jet as a result of the inflow boundary condition, which seems to contribute to its spreading.
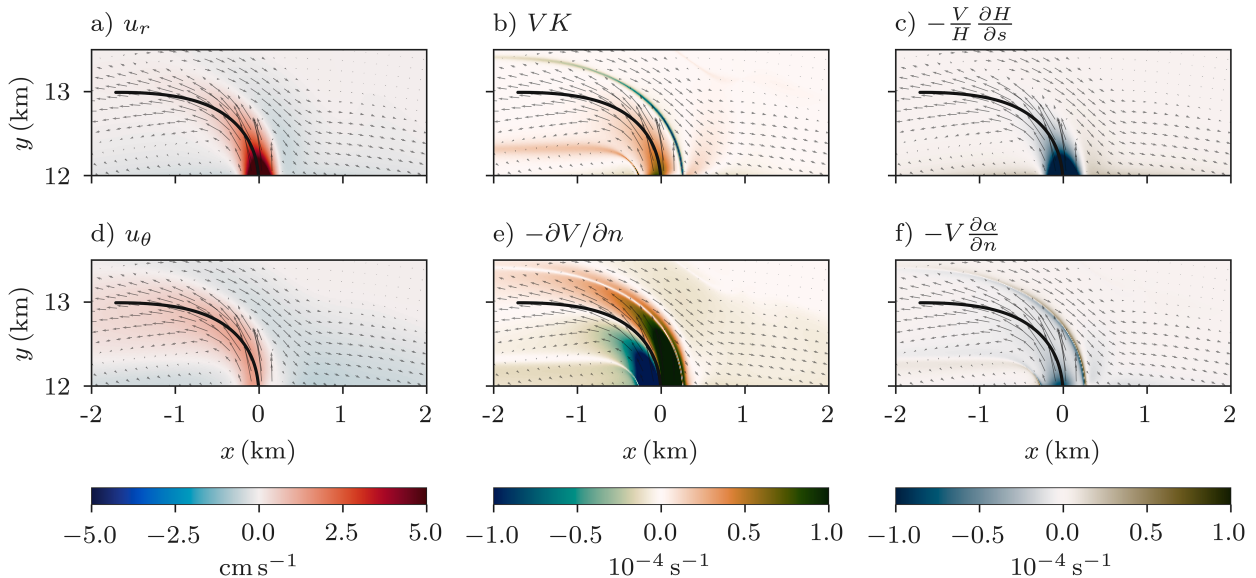
FIG. 6. Fields from a demonstrative simulation where $\phi = -30°$, $\Lambda = 0.1$, and $C_D = 0.125$. (a) Radial velocity component in island coordinates. (b) Curvature component of vertical vorticity. (c) Topographic component of divergence. (d) Azimuthal velocity component in island coordinates. (e) Shear component of vertical vorticity. (f) Diffluence component of divergence. Vectors indicate depth-integrated transport.

## b. Vorticity and divergence

Recall that the vorticity of any flow can be decomposed into shear ($-\partial V/\partial n$) and curvature ($VK$) components [(7)]. In the jet, shear vorticity of opposite signs is present on opposing sides of the center streamline (Fig. 6e), while the curvature vorticity of the feature indicates the sign and intensity of its deflection (Fig. 6b). The shear vorticity weakens as the jet spreads and the spanwise length scale increases, with clear minima along the centerline. The smoothly varying and consistently positive sign of curvature vorticity is consistent with the jet coherently deflecting anticlockwise, relaxing as it transitions into a far-field coastal current. The along-centerline curvature vorticity begins in inertial balance ($VK \approx f$) and dominates over the shear vorticity throughout the near field of the trajectory for ~1.3 km. As the flow orients to isobaths, the curvature vorticity approaches the topographic curvature vorticity set by the island geometry (Fig. 7b). As long as the curvature vorticity dominates over the shear vorticity, the simplifications required arrive at the simplified curvature dynamics equation [(11)] and are reasonable.

The other key simplification in deriving (11) is that the volume dynamics are predominantly controlled by streamwise topographic change rather than diffluent streamlines. The rapid deceleration of the jet as it encounters the slope is clearly shown by the topographic divergence (Fig. 6c), while the weak, but steady spreading of the jet can be attributed to diffluence divergence (Fig. 6f). The topographic component dominates for about 1 km along the center streamline as the jet aligns toward isobaths until it no longer experiences a streamwise depth gradient (Fig. 7a). Thus, the assumption $\Upsilon \gg 1$ is most valid in the jet near field. It is apparent that the assumptions about the divergence and vorticity

components requisite for the simplified model are most valid in the near field of the jet. This is consistent with the adherence of the ODE system trajectories to the 2D numerical model in the near field of the jet and less congruence in the far field (Figs. 4 and 5). In summary, the terms involving curvature/shear vorticity and topographic/diffluence divergence dominate in the near field and far field of the jet, respectively (Fig. 7).

## c. Curvature dynamics

Having justified the simplifications required to derive the reduced physics model in the near field of the jet, we can explicitly examine the curvature dynamics. By examining the leading-order balances, we can gain physical intuition into the mechanisms by which the jet is deflected, with the terms readily interpreted as directing the curvature of the center streamline one way or another. Along the jet center streamline in the representative case, the leading-order near-field balance is between the curvature and Coriolis stretching terms, slope torque, and curvature dissipation (Fig. 8). In this region ($s \leq 500$ m), the jet's curvature increases after emerging in nearly inertial balance (Fig. 7). As the jet moves offshore, curvature stretching turns the jet anticlockwise in the same direction of its initial curvature. The Coriolis stretching term opposes the curvature stretching term, nudging the jet toward inertial balance. The two important effects of bottom drag in the near field are the slope torque and curvature dissipation. Slope torque arises because the jet exits at a slight angle relative to isobath normals and contributes to the anticlockwise deflection of the jet. Curvature dissipation relaxes the curvature of the jet and incidentally increases its offshore excursion scale. The net effect of the bottom drag terms, however, is not particularly substantial in this case. Note that the
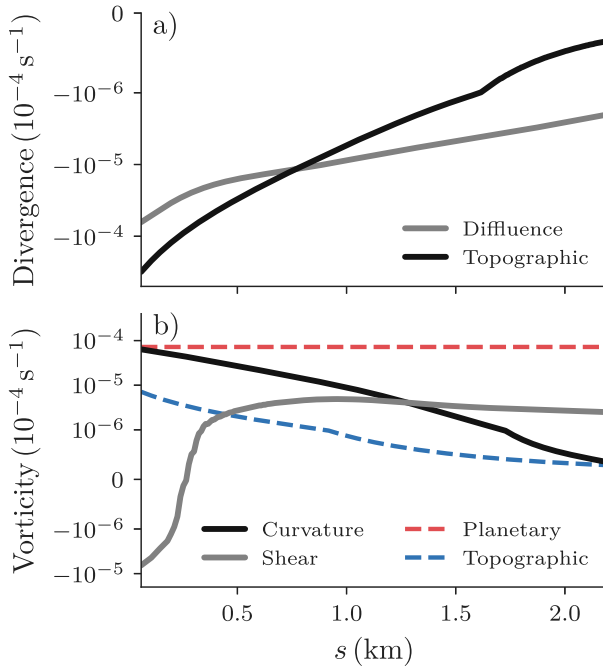
FIG. 7. The along-jet center streamline balances of the contributions to (a) the divergence and (b) the relative vorticity for a demonstrative simulation ($\phi = -30°$, $\Lambda = 0.1$, and $C_D = 0.125$) decomposed into diffluence/topographic and shear/curvature components, respectively. The curvature vorticity starts in balance with the planetary vorticity ($-f$) and asymptotes to the topographic curvature vorticity $VK_i$ in the far field, aligning with isobaths. These terms were computed as a gridded product from the model output following (A3)–(A6) and then interpolated onto the jet center streamline as identified by (16).

dominant terms in the near field are exactly the four terms identified by the reduced physics model [(11)], confirming the validity of the ODE system under these conditions.

On both flanks of the jet, shear divergence is primarily in balance with the speed torque and shear stretching terms (Fig. 9). The sign of the shear divergence is consistent with the jet spreading (i.e., attenuation of the spanwise shear). Speed torque acts to spread the jet, while shear stretching opposes it, especially in the near field when the jet is normally incident to isobaths. Confluence veering and shear divergence are strong at the jet–ambient interface, across which the velocity reverses direction and streamlines deflect (Fig. 9).

We now consider curvature dynamics variation across the parameter space. The curvature gradient flux [$V(\partial K/\partial s)$] exhibits a similar pattern across cases, decaying with the streamwise distance, but the dynamical balances can be different (Fig. 10). For intermediate and steep slopes ($\Lambda = [0.05, 0.1]$), the jet initially gains anticlockwise curvature due to curvature stretching and then loses its curvature due to planetary rotation and bottom drag as the jet aligns toward isobaths. For shallow slopes, positive curvature gradient flux is driven by confluence veering and shear divergence in the near field and speed torque in the far field, balanced by the Coriolis stretching and curvature dissipation throughout. After

normalization by $f$, all of these dynamics are consistent across different latitudes. Although the inflow boundary condition on either side of the jet induces some spreading, the centerline path is not obviously affected by this. In fact, for the high slope/high rotation cases with the most pronounced return flows, confluence veering is minimal. Confluence veering is the candidate mechanism by which jet spreading can influence the curvature gradient flux and consequently the jet's trajectory.

As the spreading of the jet is enhanced over shallower slopes (Fig. 4), confluence veering becomes progressively more important (Fig. 10). Speed torque and shear divergence also become increasingly important in the near field of jets on shallower slopes, for which the centerline is not as distinct. Shear and spreading are neglected in the reduced physics model. Speed torque and shear divergence are often inversely proportional to another, but speed torque remains relevant in the far field while shear divergence does not. Instead, the Coriolis stretching and curvature dissipation balance against speed torque in the far field. This implies that the streamwise shear variation is related to the Coriolis acceleration and bottom slope and inversely to bottom drag. In other words, the vorticity acquisition due to friction and sloped topography occurs in the shear vorticity components rather than the curvature components for lower slope cases. Shear stretching, horizontal viscosity, and unsteadiness are negligible along the jet streamline.

For weak slopes and negligible rotation, the jets do not curve much, and therefore, the centerline streamwise curvature gradient flux is weak. The difference in vorticity generated and dissipated by topographic stretching and speed torque results in the streamwise modification of the shear profile of the jet instead of curvature. In the absence of rotation for an outflow with negligible curvature, (10) collapses to a balance between shear divergence, shear stretching, and speed torque:

$$\frac{\partial}{\partial s}\frac{\partial V}{\partial n} = \frac{\Lambda - 2C_D}{H}\frac{\partial V}{\partial n}. \tag{17}$$

In the slope-dominated regime ($\Lambda \gg C_D$), this is analogous to the potential vorticity conservation with no planetary acceleration or curvature vorticity where the jet will stretch and narrow (Bowen 1969). Conversely, in a frictionally dominated regime ($C_D \gg \Lambda$), the shear vorticity can only decrease and the jet will widen.

## 5. Discussion

### a. Jet behavior and classification

Here, we relate jet behavior to the nondimensional parameters governing jet deflection dynamics. From (4), a frictional (or equivalent) Reynolds number [$\mathrm{Re}_f = H/(C_D L_J)$] arises after taking the ratio of the nonlinear advection and bottom drag terms (Pingree and Maddock 1980), where $L_J$ is the pathlength of the jet. From (5), a jet Rossby number arises [$\mathrm{Ro}_J = q_0 K/(Hf)$], where $K$ is the curvature of the jet. The jet's near-field curvature $K$ is assumed to scale with $L_J^{-1}$. The depth is assumed to scale the near field with the bottom slope, $H \sim L_J\Lambda$. Now, an Ekman number (Ek) can be formed,
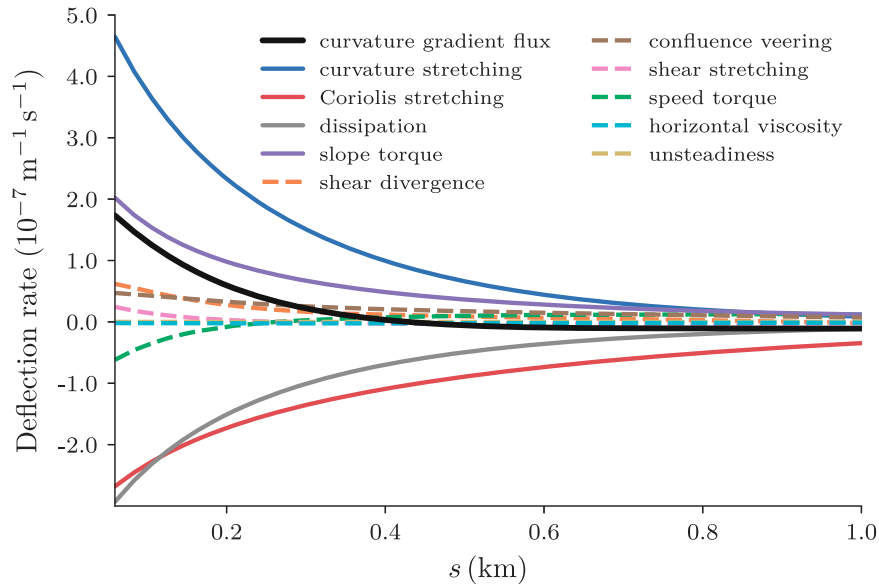
Fig. 8. The along-jet center streamline balances of the curvature dynamics equation terms [(10)]. The solid lines are the terms included in the 1D reduced physics model [(13)], while the dashed lines are not. The effects of unsteadiness and horizontal viscosity are also included as they are present in the 2DH model, albeit negligible along the center streamline. These terms were computed as a gridded product from the model output and then interpolated onto the jet center streamline as identified by (16). Residuals between curvature gradient flux reconstructed from the terms in (10) and directly computed curvature gradient flux are negligible.

which assesses the relative importance of friction to planetary rotation:

$$\text{Ek} = \frac{\text{Ro}_J}{\text{Re}_f} \approx \frac{q_0 C_D}{f L_j^2 \Lambda} \sim \frac{\text{bottom drag}}{\text{planetary rotation}}. \tag{18}$$

We find that the relative cross-shelf penetration distance of the jet $L_p$ is proportional to the Ekman number (Fig. 11), which assesses the relative importance of planetary rotation versus bottom drag. Planetary rotation influences the jet penetration distance unless bottom drag dominates. In small Ekman number scenarios (Ek < 1), Coriolis acceleration deflects the jet and restricts its cross-shelf extent. Large Ekman number scenarios (Ek > 1) are associated with weak rotation, weak slope, and high drag conditions which are more conducive to spreading rather than deflection as in (17). The degree of spreading should also influence the strength of the jet at its cross-shelf extent and potentially its robustness to deflection by alongshore crossflows like tides (Jones et al. 2007; Basdurak et al. 2020). We leave further investigation of jet spreading to future research.

The curvature of the coastline ($K_i$) may also affect the behavior of the jet. Bathymetric curvature and planetary rotation set a shallow bound on the isobath upon which the jet can settle into a coastal current. On a circular island, the coastal current could be in cyclogeostrophic balance for a topographic Rossby number of unity $VK_i/f \lesssim 1$. If we assume negligible spreading, ($Q_i = V_0 h_0 w_0 = V_i h_i w_0$) and $h_i \approx \Lambda/K_i$, then the topographic Rossby number of the coastal current is $\text{Ro}_i = q_0 K_i^2/(\Lambda f)$. In the steep slope/high Coriolis case examined here, the minimum radius of curvature for $\text{Ro}_i = 1$ would be $R_i > 400$ m, which is much smaller than the radius of the island and even the width of the jet. Therefore, our case would likely resemble a coastline with no curvature. This scale, however, is on the order of alongcoast features such as headlands and embayments, which are well known to affect the path of alongshore currents and can induce secondary circulation patterns (Geyer 1993; Garrett 1995; Castelao and Barth 2006; Whitney 2023).

### b. Extension of curvature dynamics to buoyant flows

Although barotropic outflows are the focus of this study, many coastal outflows possess a horizontal difference between the surrounding ocean, e.g., rivers, tidal estuarine plumes, and thermal/wastewater effluents (Jones et al. 2007; Horner-Devine et al. 2015; Basdurak et al. 2020). In the depth-averaged vorticity context used here, the baroclinic vorticity generation vector does not have a component in the vertical direction under the Boussinesq approximation (More and Ardekani 2023). Yet the streamnormal variation of a streamwise baroclinic pressure gradient can facilitate shear–curvature vorticity interchange without changing the total vorticity (Bell and Keyser 1993). Also, lateral buoyancy gradients induce plume spreading, which could modify the flow curvature via the confluence veering term $[VK(\partial\alpha/\partial n)]$. River plumes are known to spread transversely at the internal gravity wave speed at their edge ($u = \sqrt{g'h}$) (Hetland and MacDonald 2008). The diffluence angle can be approximated as the difference between the plume center and the edge streamline orientation, $\tan\Delta\alpha = u/v = \text{Fr}^{-1}$ (McCabe et al. 2009). Using this simple approximation, we can coarsely approximate how buoyancy alone could affect flow curvature.
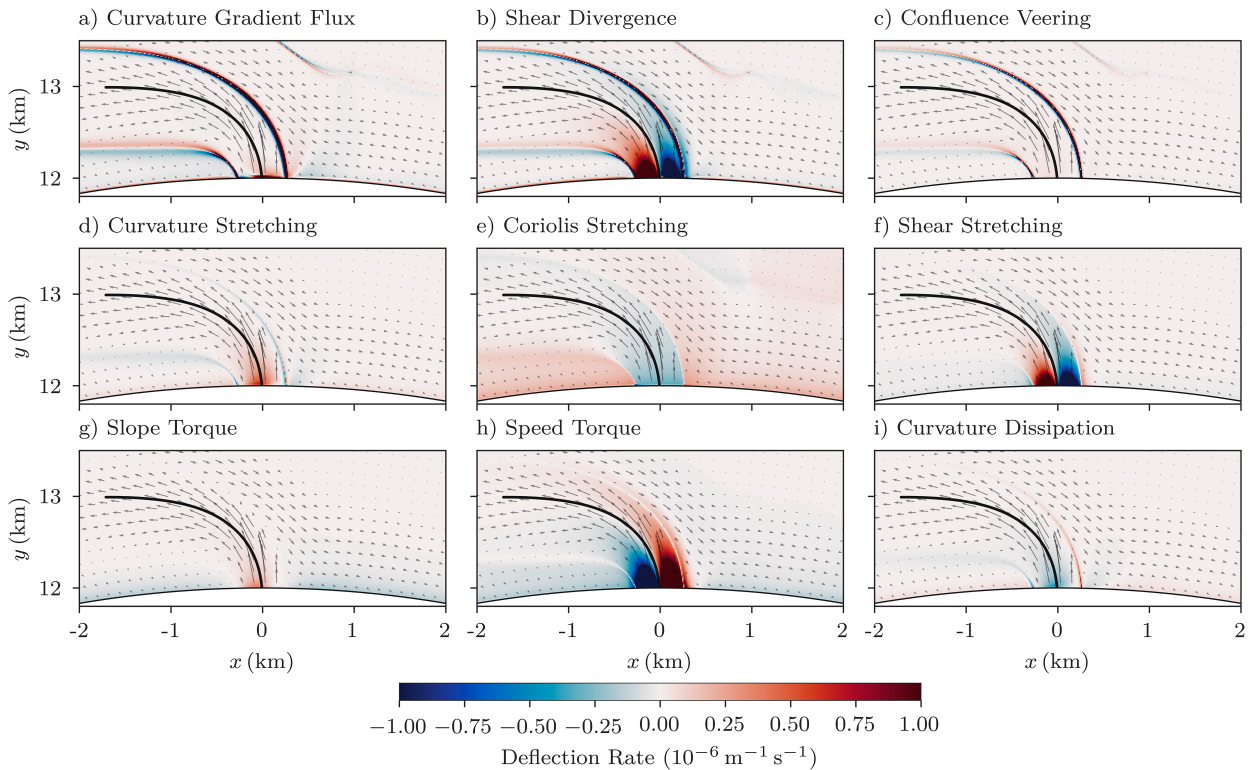
a) Curvature Gradient Flux     b) Shear Divergence     c) Confluence Veering

d) Curvature Stretching     e) Coriolis Stretching     f) Shear Stretching

g) Slope Torque     h) Speed Torque     i) Curvature Dissipation

$-1.00$  $-0.75$  $-0.50$  $-0.25$  $0.00$  $0.25$  $0.50$  $0.75$  $1.00$

Deflection Rate ($10^{-6}$ m$^{-1}$ s$^{-1}$)

FIG. 9. (a)–(i) All curvature dynamics terms [(10)] displayed across a subset of the model domain for the representative case. The curvature gradient flux in (a) is the sum of (b)–(i). Lateral momentum diffusion is ignored as it is only appreciable at the jet boundaries. The $\beta$ effect is not shown because this domain is on an $f$ plane. The unsteady curvature term is negligible and therefore not shown. Computation of the terms from the gridded model output is described in the appendix.

Assuming a balance between the curvature gradient flux and a linearized confluence veering term produces

$$\frac{1}{K}\frac{\partial K}{\partial s} \approx \frac{\text{arctanFr}^{-1}}{W}.$$

Assuming Fr is constant and applying a Taylor expansion to the half-width $W(s) = W_0 + \text{Fr}^{-1}s$ [Hetland (2010) shows $\partial W/\partial s = \text{Fr}^{-1}$] gives

$$K(s) = \frac{K_0}{W_0^\gamma}(W_0 + \text{Fr}^{-1}s)^\gamma, \tag{19}$$

where $\gamma = \text{Fr arctanFr}^{-1}$. The spreading angle is relatively small for $\gamma \to 1$. This is an oversimplification for environmental plumes but at least suggests how buoyancy-driven spreading might produce flow curvature. For supercritical flows (Fr > 1), where this spreading model is valid, the streamline curvature increases progressively less with higher Fr [for Fr $\to\infty$, $K(s) = K_0$]. Increasing the initial plume width also reduces the sensitivity of $K(s)$ to Fr.

## 6. Summary

We derived the general form of the curvature dynamics equation and used it to study the deflection and spreading of an idealized barotropic jet outflow on an idealized coast. By integrating along the center streamline and assuming a bathymetric profile, we were able to use the curvature dynamics equation to develop a 1D ODE system along the center streamline coordinate that effectively predicted the near-field trajectory of the jet when compared against 2D numerical solutions of the governing equations. The key assumptions made in deriving the reduced physics model, minimal shear vorticity, and weak diffluence relative to topographic divergence along the center streamline were verified in the near field of the jet but not in the far field after the jet had oriented itself along isobaths. Prior simplified kinematic models of barotropic outflow jets break down in the near-field region (Beardsley and Hart 1978), where the ODE system developed here is especially accurate.

Consideration of the outflow's curvature dynamics particularly clarified the role of the Coriolis–topographic interaction in steering the jet. A barotropic flow stretching vertically as it flows across a steep slope will experience an along-streamline curvature gradient flux. Thus, rather than following a steady inertial trajectory, the jet's curvature is enhanced in the near field due to vortex stretching before being rectified to isobaths by Coriolis acceleration and bottom drag. The relaxation of curvature in the near-field to far-field transition, requisite for the jet to rectify to isobaths as a coastal current, can therefore be attributed to the Coriolis stretching and curvature dissipation. In the far field, the jet reached a
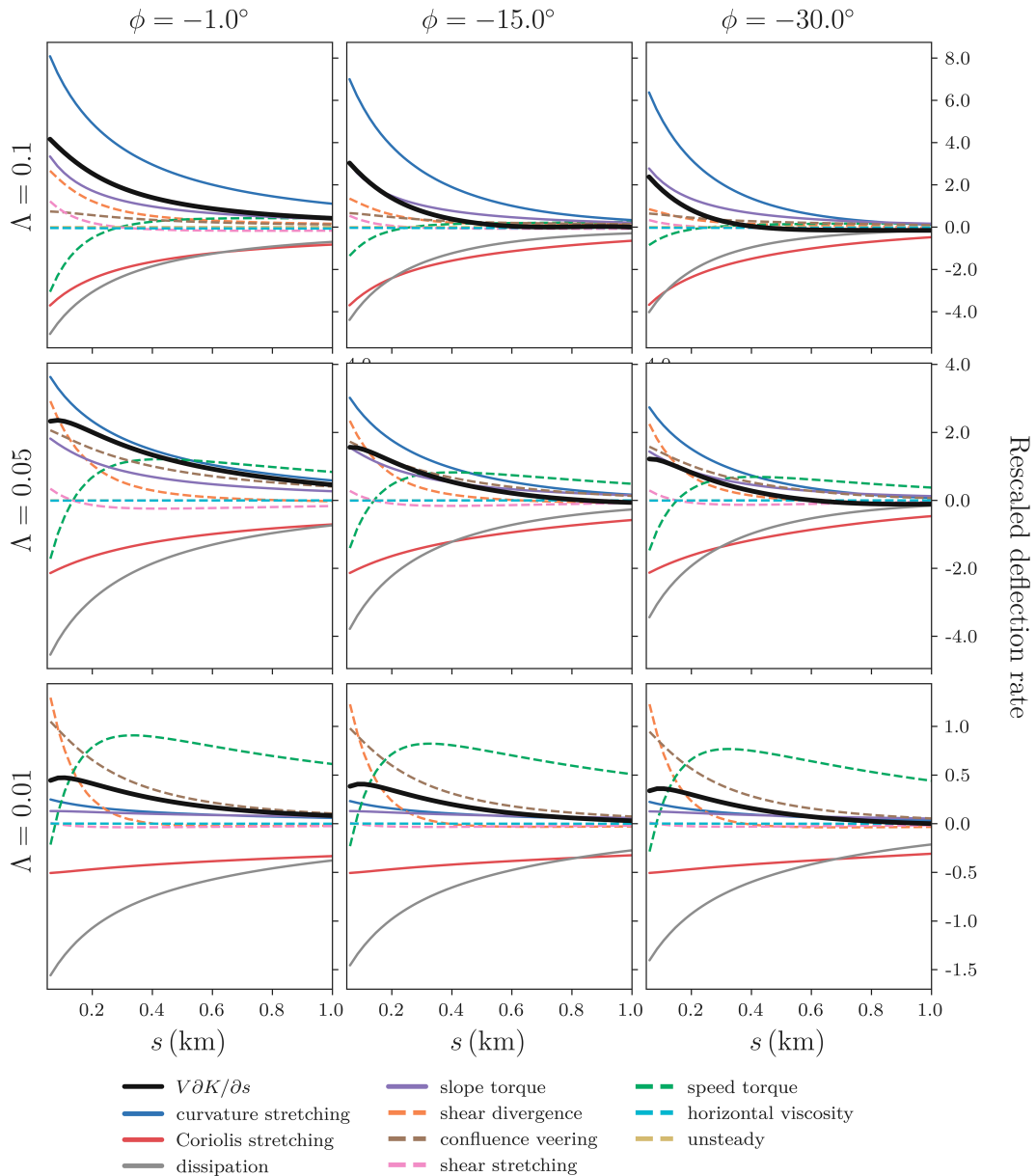
FIG. 10. The along-jet center streamline balances of the curvature dynamics terms [(10)] are compared for simulations across which the latitude and slope were varied while holding $C_D = 0.125$ constant. To facilitate comparison, the terms were rescaled by $L_J/f$, the ratio of the streamwise jet length over this section $L_J = 1$ km to the Coriolis parameter. The curvature dynamics budgets for the $C_D = 0.25$ cases are not shown because the patterns were similar besides the drag terms increasing. The solid lines are the terms included in the 1D reduced physics model [(13)], while the dashed lines are not. Curvature dynamics terms were computed from the gridded model output and then interpolated onto the jet center streamline as identified by (16).

quasi-steady state where the flow curvature approaches that of the topography and along-stream variation of flow properties is minimal.

Prior applications of curvature dynamics have generally been presented in a simplified form in oceanographic studies. Ochoa and Niiler (2007), for instance, consider a balance between curvature gradient flux and the Beta effect, finding a strong agreement with the path of the Agulhas Current. Niiler

and Robinson (1967) consider a balance between advective, topographic, and rotational effects as a model for the Gulf Stream, and Chew (1974) additionally incorporates vortex tilting and shear vorticity effects on curvature to study drogue paths in the Gulf of Mexico Loop Current, but neither study accounted for bottom drag. To our knowledge, outflow jets have not yet been analyzed from a curvature dynamics perspective. In this application, topography, advection, drag,
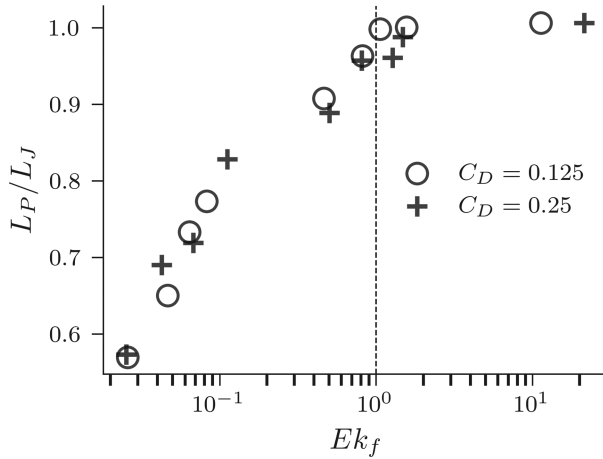
FIG. 11. Normalized cross-shore penetration distance of the jet ($L_p/L_J$) at $s = 1850$ m as a function of the Ekman number for all model simulations. The dashed vertical line indicates Ek = 1.

rotation, and shear terms can all be of leading order and must be considered to explain the behavior of the flow. The more general and inclusive dynamics captured in (10) can therefore be used to better understand more complex coastal circulation patterns.

It was found that even over relatively small $\mathcal{O}(1)\,$km scales at low latitudes, flows over steep slopes can deflect dramatically due to planetary rotation. This scale is on the order of observed excursion distances; reef pass jets may extend several kilometers into the coastal ocean (Herdman et al. 2017), while rip currents and tidal jets can reach $\mathcal{O}(1)\,$km (Short 2007; Spydell et al. 2015). Deflection of the outflow results in persistent alongshelf transport in the direction of the topographic Kelvin wave propagation, even for nearshore processes not typically assumed to be affected by planetary rotation. Deflection was also shown to reduce the cross-shelf penetration of the jet, limiting the scale of nearshore–coastal ocean exchange. Better understanding of the nonlinear dynamics that govern the transition from an outflow jet to a coastal current may aid interpretation and prediction of dispersion, retention, export, and connectivity patterns, and coastal exchange processes in general.

## APPENDIX

### Computing Curvature Dynamics Equation Terms in Cartesian Coordinates

The streamwise–streamnormal coordinate system is useful for examining the flow curvature dynamics, but computing the constituent terms from field observations or gridded model output is not straightforward. Here, we present curvature dynamics equation terms in Cartesian coordinates to facilitate application. Expressing $(s, n)$ derivatives in $(x, y)$ terms gives

$$\frac{\partial}{\partial s} = \frac{u}{V}\frac{\partial}{\partial x} + \frac{v}{V}\frac{\partial}{\partial y}, \qquad (A1)$$

$$\frac{\partial}{\partial n} = -\frac{v}{V}\frac{\partial}{\partial x} + \frac{u}{V}\frac{\partial}{\partial y}. \qquad (A2)$$

The reader is referred to Bell and Keyser (1993) for details about mathematical identities and operations in the natural coordinate system. It is helpful to compute certain intermediate quantities first.

(i) Curvature

$$\frac{\partial \alpha}{\partial s} = \frac{1}{V^2}\left[u^2\frac{\partial v}{\partial x} - v^2\frac{\partial u}{\partial x} - uv\left(\frac{\partial u}{\partial x} - \frac{\partial v}{\partial y}\right)\right]. \qquad (A3)$$

(ii) Confluence/diffluence

$$\frac{\partial \alpha}{\partial n} = \frac{1}{V^3}\left[u^2\frac{\partial v}{\partial y} + v^2\frac{\partial u}{\partial x} - uv\left(\frac{\partial v}{\partial x} + \frac{\partial u}{\partial y}\right)\right]. \qquad (A4)$$

(iii) Divergence

$$\frac{\partial V}{\partial s} = \frac{1}{V^2}\left[u^2\frac{\partial u}{\partial x} + v^2\frac{\partial v}{\partial y} + uv\left(\frac{\partial v}{\partial x} + \frac{\partial u}{\partial y}\right)\right]. \qquad (A5)$$

(iv) Streamnormal shear

$$\frac{\partial V}{\partial n} = \frac{1}{V^2}\left[u^2\frac{\partial u}{\partial y} + v^2\frac{\partial v}{\partial x} - uv\left(\frac{\partial u}{\partial x} - \frac{\partial v}{\partial y}\right)\right]. \qquad (A6)$$

Equations (A3)–(A6) can be used to compute the vorticity and divergence components as in (7) and (8). After additionally computing the first- and second-order velocity derivatives, it is possible to directly compute the streamwise curvature gradient and shear divergence in Cartesian coordinates.

(v) Streamwise curvature gradient

$$\frac{\partial K}{\partial s} = \frac{u}{V^4}\left[u^2\frac{\partial^2 v}{\partial x^2} + 2u\frac{\partial u}{\partial x}\frac{\partial v}{\partial x} - v^2\frac{\partial^2 u}{\partial x\partial y} - 2v\frac{\partial v}{\partial x}\frac{\partial u}{\partial y} - \left(u\frac{\partial v}{\partial x} + v\frac{\partial u}{\partial x}\right)\left(\frac{\partial u}{\partial x} - \frac{\partial v}{\partial y}\right) - uv\left(\frac{\partial^2 u}{\partial x^2} - \frac{\partial^2 v}{\partial x\partial y}\right)\right]$$

$$+ \frac{v}{V^4}\left[u^2\frac{\partial^2 v}{\partial x\partial y} + 2u\frac{\partial u}{\partial y}\frac{\partial v}{\partial x} - v^2\frac{\partial^2 u}{\partial y^2} - 2v\frac{\partial u}{\partial y}\frac{\partial v}{\partial y} - \left(u\frac{\partial v}{\partial y} + v\frac{\partial u}{\partial x}\right)\left(\frac{\partial u}{\partial x} - \frac{\partial v}{\partial y}\right) - uv\left(\frac{\partial^2 u}{\partial x\partial y} - \frac{\partial^2 v}{\partial y^2}\right)\right]$$

$$- 3K\left(\frac{u}{V^2}\frac{\partial V}{\partial x} + \frac{v}{V^2}\frac{\partial V}{\partial y}\right). \tag{A7}$$

(vi) Shear divergence

$$\frac{\partial}{\partial s}\frac{\partial V}{\partial n} = \frac{u}{V^3}\left[u^2\frac{\partial^2 u}{\partial x\partial y} + 2u\frac{\partial u}{\partial x}\frac{\partial u}{\partial y} - v^2\frac{\partial^2 v}{\partial x^2} - 2v\left(\frac{\partial v}{\partial x}\right)^2 - uv\left(\frac{\partial^2 u}{\partial x^2} - v\frac{\partial^2 v}{\partial x\partial y}\right) - \left(u\frac{\partial v}{\partial x} + v\frac{\partial u}{\partial x}\right)\left(\frac{\partial u}{\partial x} - \frac{\partial v}{\partial y}\right)\right]$$

$$+ \frac{v}{V^3}\left[u^2\frac{\partial^2 u}{\partial y^2} + 2u\left(\frac{\partial u}{\partial y}\right)^2 - v^2\frac{\partial^2 v}{\partial x\partial y} - 2v\frac{\partial v}{\partial x}\frac{\partial v}{\partial y} - uv\left(\frac{\partial^2 u}{\partial x\partial y} - v\frac{\partial^2 v}{\partial y^2}\right) - \left(u\frac{\partial v}{\partial y} + v\frac{\partial u}{\partial y}\right)\left(\frac{\partial u}{\partial x} - \frac{\partial v}{\partial y}\right)\right]$$

$$- 2\frac{\partial V}{\partial n}\left(\frac{u}{V^2}\frac{\partial V}{\partial x} + \frac{v}{V^2}\frac{\partial V}{\partial y}\right). \tag{A8}$$

The final required terms are the Cartesian depth gradient and the streamwise Coriolis parameter gradient if applicable. Using (A1) and (A2)

$$\left(\frac{\partial H}{\partial s}, \frac{\partial H}{\partial n}\right) = \left(\frac{u}{V}\frac{\partial H}{\partial x} + \frac{v}{V}\frac{\partial H}{\partial y}, -\frac{v}{V}\frac{\partial H}{\partial x} + \frac{u}{V}\frac{\partial H}{\partial y}\right), \tag{A9}$$

$$\frac{\partial f}{\partial s} = \frac{u}{V}\frac{\partial f}{\partial x} + \frac{v}{V}\frac{\partial f}{\partial y}. \tag{A10}$$

After combining (A3)–(A10), each component of the curvature dynamics equation may be computed directly from the Cartesian velocity components and their derivatives which can be discretized using standard finite-difference methods:

$$V\frac{\partial K}{\partial s} = \frac{\partial}{\partial s}\frac{\partial V}{\partial n} + VK\frac{\partial \alpha}{\partial n} + \frac{\partial f}{\partial s} + \frac{1}{H}\frac{\partial H}{\partial s}\left(-\frac{\partial V}{\partial n} + 2VK + f\right)$$

$$+ \frac{C_D}{H}\left(-\frac{V}{H}\frac{\partial H}{\partial n} + 2\frac{\partial V}{\partial n} - VK\right). \tag{A11}$$

## REFERENCES

An, B. W., and N. R. McDonald, 2004: Coastal currents generated by outflow and vorticity and their interaction with topography. *Cont. Shelf Res.*, **24**, 1531–1547, https://doi.org/10.1016/j.csr.2004.05.002.

Arfken, G. B., H. J. Weber, and F. E. Harris, 2013: Ordinary differential equations. *Mathematical Methods for Physicists*, 7th ed. G. B. Arfken, H. J. Weber, and F. E. Harris, Eds., Academic Press, 329–380, https://doi.org/10.1016/B978-0-12-384654-9.00007-4.

Atkinson, J. F., 1993: Detachment of buoyant surface jets discharged on slope. *J. Hydraul. Eng.*, **119**, 878–894, https://doi.org/10.1061/(ASCE)0733-9429(1993)119:8(878).

Basdurak, N. B., J. L. Largier, and N. J. Nidzieko, 2020: Modeling the dynamics of small-scale river and creek plumes in tidal waters. *J. Geophys. Res.: Oceans*, **125**, e2019JC015737, https://doi.org/10.1029/2019JC015737.

Beardsley, R. C., and J. Hart, 1978: A simple theoretical model for the flow of an estuary onto a continental shelf. *J. Geophys. Res.*, **83**, 873–883, https://doi.org/10.1029/JC083iC02p00873.

Bell, G. D., and D. Keyser, 1993: Shear and curvature vorticity and potential-vorticity interchanges: Interpretation and application to a cutoff cyclone event. *Mon. Wea. Rev.*, **121**, 76–102, https://doi.org/10.1175/1520-0493(1993)121<0076:SACVAP>2.0.CO;2.

Bowen, A. J., 1969: Rip Currents: 1. Theoretical investigations. *J. Geophys. Res.*, **74**, 5467–5478, https://doi.org/10.1029/JC074i023p05467.

Brun, A. A., N. Ramirez, O. Pizarro, and A. R. Piola, 2020: The role of the Magellan Strait on the southwest South Atlantic shelf. *Estuarine Coastal Shelf Sci.*, **237**, 106661, https://doi.org/10.1016/j.ecss.2020.106661.

Castelao, R. M., and J. A. Barth, 2006: The relative importance of wind strength and along-shelf bathymetric variations on the separation of a coastal upwelling jet. *J. Phys. Oceanogr.*, **36**, 412–425, https://doi.org/10.1175/JPO2867.1.

Castelle, B., T. Scott, R. W. Brander, and R. J. McCarroll, 2016: Rip current types, circulation and hazard. *Earth-Sci. Rev.*, **163**, 1–21, https://doi.org/10.1016/j.earscirev.2016.09.008.

Chew, F., 1974: The turning process in meandering currents: A case study. *J. Phys. Oceanogr.*, **4**, 27–57, https://doi.org/10.1175/1520-0485(1974)004<0027:TTPIMC>2.0.CO;2.

——, 1975: The interaction between curvature and lateral shear vorticities in a mean and an instantaneous Florida current, a comparison. *Tellus*, **27A**, 606–618, https://doi.org/10.3402/tellusa.v27i6.10187.

Cole, K. L., and R. D. Hetland, 2016: The effects of rotation and river discharge on net mixing in small-mouth Kelvin number plumes. *J. Phys. Oceanogr.*, **46**, 1421–1436, https://doi.org/10.1175/JPO-D-13-0271.1.

Cushman-Roisin, B., J. A. Proehl, and D. T. Morgan, 1997: Barotropic thin jets over arbitrary topography. *Dyn. Atmos. Oceans*, **26**, 73–93, https://doi.org/10.1016/S0377-0265(96)00484-8.

Delandmeter, P., and E. van Sebille, 2019: The parcels v2.0 Lagrangian framework: New field interpolation schemes. *Geosci. Model Dev.*, **12**, 3571–3584, https://doi.org/10.5194/gmd-12-3571-2019.

Flexas, M. M., G. J. F. van Heijst, and R. R. Trieling, 2005: The behavior of jet currents over a continental slope topography with a possible application to the northern current. *J. Phys. Oceanogr.*, **35**, 790–810, https://doi.org/10.1175/JPO2705.1.

Flierl, G. R., 1999: Thin jet and contour dynamics models of Gulf Stream meandering. *Dyn. Atmos. Oceans*, **29**, 189–215, https://doi.org/10.1016/S0377-0265(99)00006-8.

Garrett, C., 1995: Flow separation in the ocean. *Proc. Eighth 'Aha Huliko'a Hawaiian Winter Workshop*, Honolulu, HI, SOEST Special Publication, 119–124, https://www.soest.hawaii.edu/PubServices/1995pdfs/Garrett.pdf.

Geyer, W. R., 1993: Three-dimensional tidal flow around headlands. *J. Geophys. Res.*, **98**, 955–966, https://doi.org/10.1029/92JC02270.

Hench, J. L., and R. A. Luettich Jr., 2003: Transient tidal circulation and momentum balances at a shallow inlet. *J. Phys. Oceanogr.*, **33**, 913–932, https://doi.org/10.1175/1520-0485(2003)33<913:TTCAMB>2.0.CO;2.

——, J. J. Leichter, and S. G. Monismith, 2008: Episodic circulation and exchange in a wave-driven coral reef and lagoon system. *Limnol. Oceanogr.*, **53**, 2681–2694, https://doi.org/10.4319/lo.2008.53.6.2681.

Herdman, L. M. M., J. L. Hench, O. Fringer, and S. G. Monismith, 2017: Behavior of a wave-driven buoyant surface jet on a coral reef. *J. Geophys. Res. Oceans*, **122**, 4088–4109, https://doi.org/10.1002/2016JC011729.

Hetland, R. D., 2010: The effects of mixing and spreading on density in near-field river plumes. *Dyn. Atmos. Oceans*, **49**, 37–53, https://doi.org/10.1016/j.dynatmoce.2008.11.003.

——, and D. G. MacDonald, 2008: Spreading in the near-field Merrimack River plume. *Ocean Modell.*, **21**, 12–21, https://doi.org/10.1016/j.ocemod.2007.11.001.

Horner-Devine, A. R., R. D. Hetland, and D. G. MacDonald, 2015: Mixing and transport in coastal river plumes. *Annu. Rev. Fluid Mech.*, **47**, 569–594, https://doi.org/10.1146/annurev-fluid-010313-141408.

Jones, G. R., J. D. Nash, R. L. Doneker, and G. H. Jirka, 2007: Buoyant surface discharges into water bodies. I: Flow classification and prediction methodology. *J. Hydraul. Eng.*, **133**, 1010–1020, https://doi.org/10.1061/(ASCE)0733-9429(2007)133:9(1010).

Kubokawa, A., 1991: On the behaviour of outflows with low potential vorticity from a sea strait. *Tellus*, **43**, 168–176, https://doi.org/10.3402/tellusa.v43i2.11924.

Kumar, N., and F. Feddersen, 2017: A new offshore transport mechanism for shoreline-released tracer induced by transient rip currents and stratification. *Geophys. Res. Lett.*, **44**, 2843–2851, https://doi.org/10.1002/2017GL072611.

Lane, E. M., J. M. Restrepo, and J. C. McWilliams, 2007: Wave–current interaction: A comparison of radiation-stress and vortex-force representations. *J. Phys. Oceanogr.*, **37**, 1122–1141, https://doi.org/10.1175/JPO3043.1.

Lemagie, E., and J. Lerczak, 2020: The evolution of a buoyant river plume in response to a pulse of high discharge from a small midlatitude river. *J. Phys. Oceanogr.*, **50**, 1915–1935, https://doi.org/10.1175/JPO-D-19-0127.1.

Lowe, R. J., and J. L. Falter, 2015: Oceanic forcing of coral reefs. *Annu. Rev. Mar. Sci.*, **7**, 43–66, https://doi.org/10.1146/annurev-marine-010814-015834.

McCabe, R. M., P. MacCready, and B. M. Hickey, 2009: Ebb-tide dynamics and spreading of a large river plume. *J. Phys. Oceanogr.*, **39**, 2839–2856, https://doi.org/10.1175/2009JPO4061.1.

More, R. V., and A. M. Ardekani, 2023: Motion in stratified fluids. *Annu. Rev. Fluid Mech.*, **55**, 157–192, https://doi.org/10.1146/annurev-fluid-120720-011132.

Moulton, M., S. H. Suanda, J. C. Garwood, N. Kumar, M. R. Fewings, and J. M. Pringle, 2023: Exchange of plankton, pollutants, and particles across the nearshore region. *Annu. Rev. Mar. Sci.*, **15**, 167–202, https://doi.org/10.1146/annurev-marine-032122-115057.

Niiler, P. P., and A. R. Robinson, 1967: The theory of free inertial jets: II. A numerical experiment for the path of the Gulf Stream. *Tellus*, **19**, 601–619, https://doi.org/10.1111/j.2153-3490.1967.tb01511.x.

Ochoa, J., and P. P. Niiler, 2007: Vertical vorticity balance in meanders downstream the Agulhas retroflection. *J. Phys. Oceanogr.*, **37**, 1740–1744, https://doi.org/10.1175/JPO3064.1.

Pingree, R. D., and L. Maddock, 1980: The effects of bottom friction and Earth's rotation on an island's wake. *J. Mar. Biol. Assoc. U. K.*, **60**, 499–508, https://doi.org/10.1017/S0025315400028514.

Quataert, E., C. Storlazzi, A. van Rooijen, O. Cheriton, and A. van Dongeren, 2015: The influence of coral reefs and climate change on wave-driven flooding of tropical coastlines. *Geophys. Res. Lett.*, **42**, 6407–6415, https://doi.org/10.1002/2015GL064861.

Rodriguez, A. R., S. N. Giddings, and N. Kumar, 2018: Impacts of nearshore wave-current interaction on transport and mixing of small-scale buoyant plumes. *Geophys. Res. Lett.*, **45**, 8379–8389, https://doi.org/10.1029/2018GL078328.

Shchepetkin, A. F., and J. C. McWilliams, 2005: The Regional Oceanic Modeling System (ROMS): A split-explicit, free-surface, topography-following-coordinate oceanic model. *Ocean Modell.*, **9**, 347–404, https://doi.org/10.1016/j.ocemod.2004.08.002.

Short, A. D., 2007: Australian rip systems – Friend or foe? *J. Coastal Res.*, **50**, 7–11, https://doi.org/10.2112/JCR-SI50-002.1.

Signell, R. P., and W. R. Geyer, 1991: Transient eddy formation around headlands. *J. Geophys. Res.*, **96**, 2561–2575, https://doi.org/10.1029/90JC02029.

Southwick, O. R., E. R. Johnson, and N. R. McDonald, 2017: Potential vorticity dynamics of coastal outflows. *J. Phys. Oceanogr.*, **47**, 1021–1041, https://doi.org/10.1175/JPO-D-16-0070.1.

Spydell, M. S., F. Feddersen, M. Olabarrieta, J. Chen, R. T. Guza, B. Raubenheimer, and S. Elgar, 2015: Observed and modeled drifters at a tidal inlet. *J. Geophys. Res. Oceans*, **120**, 4825–4844, https://doi.org/10.1002/2014JC010541.

Suanda, S. H., and F. Feddersen, 2015: A self-similar scaling for cross-shelf exchange driven by transient rip currents. *Geophys. Res. Lett.*, **42**, 5427–5434, https://doi.org/10.1002/2015GL063944.

Symonds, G., K. P. Black, and I. R. Young, 1995: Wave-driven flow over shallow reefs. *J. Geophys. Res.*, **100**, 2639–2648, https://doi.org/10.1029/94JC02736.

Talbot, M. M. B., and G. C. Bate, 1987: Rip current characteristics and their role in the exchange of water and surf diatoms between the surf zone and nearshore. *Estuarine Coastal Shelf Sci.*, **25**, 707–720, https://doi.org/10.1016/0272-7714(87)90017-5.

Thomas, P. J., and P. F. Linden, 2007: Rotating gravity currents: Small-scale and large-scale laboratory experiments and a geostrophic model. *J. Fluid Mech.*, **578**, 35–65, https://doi.org/10.1017/S0022112007004739.

Virtanen, P., and Coauthors, 2020: SciPy 1.0: Fundamental algorithms for scientific computing in Python. *Nat. Methods*, **17**, 261–272, https://doi.org/10.1038/s41592-019-0686-2.

Warren, B. A., 1963: Topographic influences on the path of the Gulf Stream. *Tellus*, **15**, 167–183, https://doi.org/10.1111/j.2153-3490.1963.tb01376.x.

Wenegrat, J. O., and L. N. Thomas, 2017: Ekman transport in balanced currents with curvature. *J. Phys. Oceanogr.*, **47**, 1189–1203, https://doi.org/10.1175/JPO-D-16-0239.1.

Whitehead, J. A., 1985: The deflection of a baroclinic jet by a wall in a rotating fluid. *J. Fluid Mech.*, **157**, 79–93, https://doi.org/10.1017/S0022112085002312.

Whitney, M. M., 2023: Separation of the Icelandic coastal current from the Reykjanes Peninsula. *Estuarine Coastal Shelf Sci.*, **280**, 108163, https://doi.org/10.1016/j.ecss.2022.108163.

Wolanski, E., 1988: Island wakes in shallow waters. *J. Geophys. Res.*, **93**, 1335–1336, https://doi.org/10.1029/JC093iC02p01335.